A study of 3-dimensional shapes of asteroid families with an application to Eos

M. Brož

Abstract

In order to fully understand shapes of asteroids families in the 3-dimensional space of the proper elements a_p, e_p, $\sin I_\mathrm{p}$ it is necessary to compare the observed asteroids with N-body simulations. To this point, we describe a rigorous yet simple method which allows for a selection of observed asteroids, assures the same size-frequency distribution of synthetic asteroids, accounts for the background population, and computes a χ^2 metric. We study Eos family as an example, and we are able to fully explain its non-isotropic features, including the distribution of pole latitudes. We confirm its age $t = (1.3 \pm 0.3)$ Gyr; while this value still scales with the bulk density, it is verified by a Monte-Carlo collisional model. The method can be applied to other populous families (Flora, Eunomia, Koronis, Hygieya, Themis, etc.).

1. Introduction

A rigorous comparison of observations vs simulations of asteroid families is rather a difficult task, especially when we look at Figure 1. Observed proper elements a_p, e_p, $\sin I_\mathrm{p}$, supplied by physical data (colour indices $a^\star$, $i - z$ in this case), show a complicated structure of Eos family, halo, together with many neighbouring families, overlapping halos, and background asteroids, of course. The hierarchical clustering method alone (HCM, Zappalà et al. (1995)) is then practically useless.

Family identification itself affects dynamical studies and *vice versa*. We would need the family to determine the initial conditions. On the other hand, we would need a dynamical study to understand where family members could be. There are several well-known weaknesses of HCM, which were demonstrated e.g. in a 'crime-scene' Fig. 8 of Nesvorný et al. (2015). The HCM needs a free parameter, either the cutoff velocity v_cutoff, or quasi-random level QRL. It is also unable to associate halos. Last but not least, the background is never precisely uniform what can be clearly see at the edges of currently stable zones, close or inside gravitational resonances, or even in stable zones where the population was deteriorated by dynamical processes in the distant past (Cybele region).

On the other hand, synthetic families evolve in the course of simulation, loose their members, consequently should a variable v_cutoff, but its optimal value is again generally unknown. No direct comparison is thus possible.

That is a motivation for our work. We describe a method suitable to study 3-dimensional shapes of asteroid families which enables a consistent fit of all proper orbital elements, including the size-frequency distribution, and non-uniform background. Because we are forced to select synthetic asteroids randomly (a Monte-Carlo approach), we can expect some stochasticity of the results.

We present an application to Eos family (family identification number, FIN = 606), one of the most studied families to date mentioned already by Hirayama (1918). Together with our previous works (Vokrouhlický et al., 2006; Brož and Morbidelli, 2013), it forms a long-term series focused on long-term evolution. We use up-to-date catalogues of proper elements (Knežević and Milani, 2003), and brand new spin data (Hanuš et al., 2018).

Let us recall Eos family is of K taxonomic type, while the background mostly C type. Mothé-Diniz et al. (2008) suggested either a partially differentiated parent body, with meteorite analogues CV, CO or R, or a undifferentiated one, with CK analogues. There was a discovery of a recent breakup of (6733) 1992 EF (Novaković and Tsirvoulis, 2014), belonging to the family core, what makes Eos even more interesting for space weathering studies, because we may see both old (1.3 Gyr) and young (4 Myr) surfaces.

2. Methods

Before we proceed with the description of the method, let us explain three problems we have to solve and describe the underlying dynamical model.

2.1. Problem 1: Selection of asteroids

In principle, we can select any subset of asteroids (e.g. by using SDSS, or WISE data) to decrease a contamination by interlopers, or an overlap with other families in the neighbourhood (Parker et al., 2008; Masiero et al., 2011). We can also simulate any subset at will, be we should check surroundings where the bodies can be scattered to, because this may be a key constraint.

For Eos family, it is easy because of its distinct K taxonomic type which is defined for our purposes in terms of the SDSS colour indices $a^* = (0.0, 0.1)$, $i - z = (-0.03, 0.08)$, and the geometric albedo $p_V > 0.07$ (if known). As a result, only 1/10th of asteroids remain, but this is still sufficient (Figure 2). Practically all families disappeared, the background is much more uniform. The only exception may be some contamination from Tirela, arising from a photometric noise on S-type asteroids, and a gap at large $\sin I_\mathrm{p} > 0.25$.

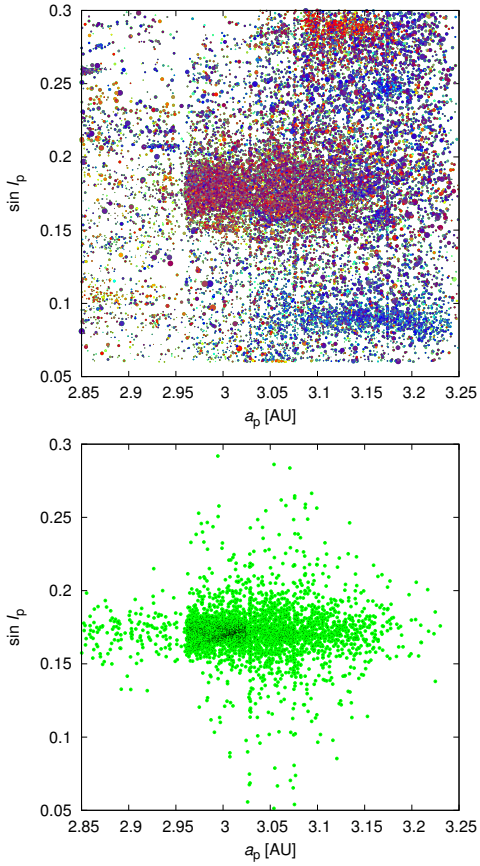

Figure 1: Top panel: the proper semimajor axis a_p vs proper inclination $\sin I_p$ for all asteroids in the broad surroundings of Eos family, and having colour data in the SDSS MOC4 catalogue (Parker et al., 2008). The range of proper eccentricities is $e_p \in (0.0; 0.3)$. Colours correspond to indices $a^\star$, $i - z$ which are closely related to taxonomy, namely blue is close to C-complex taxonomy, red to S-complex, and magenta to K-type. The whole sample contains 18 471 asteroids. There are other prominent families visible: Hygeia (C-type, bottom-right), Veritas (C, next to Eos), Tirela (S, upper right), Telramund (S, below Eos); a close inspection would show 32 families in total! Bottom panel: the same plot for a typical outcome of N-body simulations, assuming a disruption of a parent body, ejection of fragments with some velocity field, and their long-term dynamical evolution due to gravitational perturbations, resonances, chaotic diffusion, the Yarkovsky effect, the YORP effect, etc. The two panels are not directly comparable.

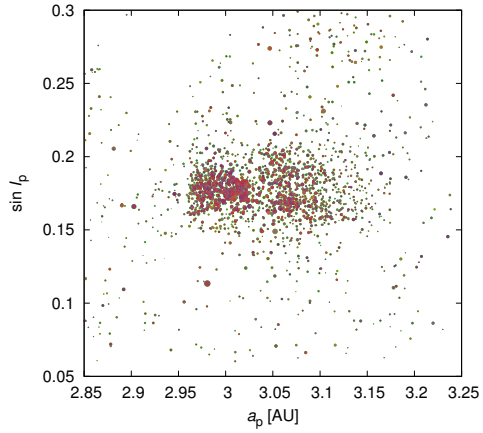

Figure 2: K-type asteroids selected from Figure 1, with known colour indices $a^* \in (0.0; 0.1)$, $i - z \in (-0.03; 0.08)$. The visual geometric albedo had to be $p_V > 0.07$ (or unknown). This subset is much more homogeneous and contains 1 991 asteroids. No other prominent families except Eos can be seen; the only exception may be some contamination by Tirela (upper right) due to inherent photometric noise. This subset seems suitable for a comparison with N-body simulations.

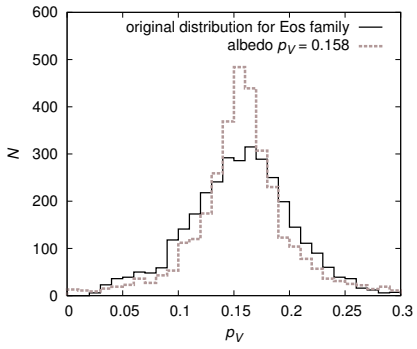

Figure 3: The observed differential distribution of visual geometric albedos p_V for Eos family from the WISE catalogue (Masiero et al., 2011) (black solid), and for the same set of bodies with p_V values assigned randomly, assuming a Gaussian distribution with a constant mean $\bar{p}_V = 0.158$, and 1-σ uncertainty declared in the catalogue (dashed gray). The widths of the two distributions are similar, so using the constant $\bar{p}_V$ (if unknown) is *not* a poor approximation.

Regarding the homogeneity of albedos, the WISE data exhibit a wide distribution. The uncertainties arise mainly from photon noise, and NEATM model systematics. From a statistical sense, even the single albedo value $\bar{p}_V = 0.158$ would result in a relatively wide distribution which is demonstrated in Figure 3. Consequently, we use this value for bodies with unknown p_V.

2.2. *Problem 2: Size-frequency distribution*

The size-frequency distributions (SFDs) should match for both the observed and synthetic populations, but the latter changes in the course of time (Figure 4). In order to compare apples with apples, we have to scale the SFD. In other words, we randomly select the same number of synthetic bodies (together with their orbits, of course) in prescribed size bins $(D, D + \mathrm{d}D)$ as the number of observed bodies. To this point, it is definitively useful to start with a larger number of synthetic

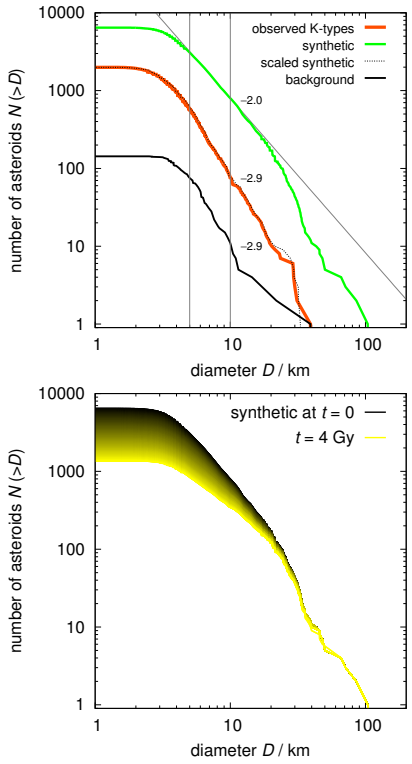

Figure 4: Top panel: the cumulative size-frequency distribution (SFD) of the observed K-type asteroids (orange), the synthetic SFD at the beginning of N-body simulation (green), the *scaled* synthetic SFD constructed by a random selection of bodies so that it matches the observed one (dotted black; hard to distinguish from orange), and the background SFD (black). Bottom panel: an evolution of the synthetic SFD in the course of an N-body simulation, from time $t = 0$ up to 4 Gyr, which is indicated by changing colours (black → yellow). These changes (due to a dynamical decay) require rescaling in every time step.

bodies, so that at the end of simulation we still have more than observed.

A random selection of synthetic asteroids is needed at every single time step of the simulation; even multiple selections at one time step are useful. This way, we would naturally account for additional (and often neglected) uncertainty which arises from the fact we always choose the bodies from some underlying distributions (e.g. from a prescribed velocity field), but we cannot be absolutely sure that our single selection is not a lucky fluke.

2.3. Problem 3: Non-uniform background

A background has to accounted for otherwise it is essentially impossible to explain a lot of bodies far from the family. First, we need to find some observed background, not very far from the family; in our case, a suitable population seems to be at $\sin I_\mathrm{p} \in (0.06; 0.12)$ and $(0.24; 0.30)$. It has its own size-frequency distribution, and we should use the same SFD for the synthetic background, of course. As a first approximation, we model the background as a random uniform distribution in the space of proper elements.

However, Murphy's law for backgrounds states: *Background is never uniform.* Especially below and above the 7/3 mean-motion resonance with Jupiter we can expect a difference (see the example in Figure 5).

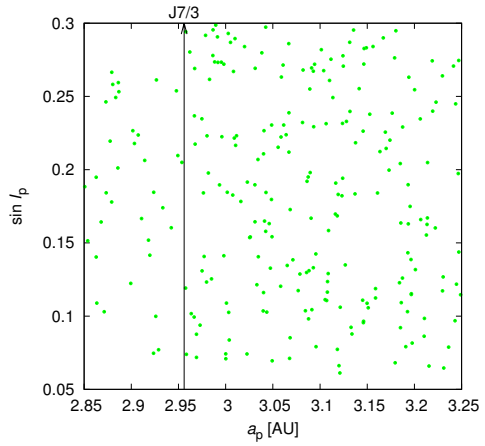

Figure 5: A synthetic background generated as a random uniform distribution in proper orbital elements $a_\mathrm{p}, e_\mathrm{p}, \sin I_\mathrm{p}$, with the same size-distribution as the observed background. In this example, the number densities below and above the 7/3 mean-motion resonance with Jupiter at 2.956 au are different (by a factor of 2), because this resonance separates two distinct zones of the main belt.

Again, there is a non-negligible stochasticity. We shall at least try different random seeds. The number density of background objects can be also treated as a free parameter. There is also *a-priori* unknown contamination by neighbouring families, because this is not necessarily present 'under' Eos family.

2.4. Dynamical model

Our dynamical model was described in detail in Brož et al. (2011). We briefly recall it contains a modified SWIFT integrator (Levison and Duncan, 1994; Laskar and Robutel, 2001), both the diurnal and seasonal Yarkovsky thermal effects (Vokrouhlický, 1998; Vokrouhlický and Farinella, 1999), which induce a semimajor axis drift $\mathrm{d}a/\mathrm{d}t$, captures in all mean-motion and secular resonances, corresponding drifts $\mathrm{d}e/\mathrm{d}t$, $\mathrm{d}I/\mathrm{d}t$, the YORP effect, $\mathrm{d}\omega/\mathrm{d}t$, $\mathrm{d}\gamma/\mathrm{d}t$ (Čapek and Vokrouhlický, 2004), with the efficiency parameter $c_\mathrm{YORP} = 0.33$ (Hanuš et al., 2011), collisional reorientations (Farinella et al., 1998), mass shedding (Pravec and Harris, 2000), and suitable digital filters for computations of mean and proper elements (Quinn et al., 1991; Šidlichovský and Nesvorný, 1996).

Initial conditions are keep as simple as possible. We assume an isotropic disruption, velocities proportional to $1/D$, with $V_5 = 93\,\mathrm{m\,s^{-1}}$ for $D_5 = 5\,\mathrm{km}$, an estimate based on our previous work (Vokrouhlický et al., 2006). We start with 6545 synthetic bodies, with the SFD covering $D \in (1.5; 100)\,\mathrm{km}$. Spins are also isotropic and periods uniform, $P \in (2; 10)\,\mathrm{h}$.

Thermal parameters remain the same as in our previous works: the bulk density $\rho = 2500\,\mathrm{kg\,m^{-3}}$, the surface density $\rho = 1500\,\mathrm{kg\,m^{-3}}$, the conductivity $K = 0.001\,\mathrm{W\,m^{-1}\,K^{-1}}$, the specific capacity $C = 680\,\mathrm{J\,kg^{-1}}$, the Bond albedo $A = 0.1$, the infrared emissivity $\epsilon = 0.9$.

Free parameters of our model are the maximum of velocity distribution v_max, the true anomaly f_imp, and the argument of pericentre ω_imp at the time of impact, which are related by

means of Gauss equations. We may forced to tune also precise orbital elements of the parent body, but for the moment we take those of (221) Eos as the nominal case.

Among fixed parameters is the bulk density ρ. Usually, the age scales linearly with ρ because of the non-gravitational accelerations. Theoretically, if there are both gravitational and non-gravitational accelerations acting at the same time (e.g. Yarkovsky drift in a and chaotic diffusion in e) we may be able to break this degeneracy. However, based on out previous experience, we do not expect this for the case of Eos. Neighbouring Veritas may be more suitable for this approach, by the way. Alternatively, we one can use collisional models which exhibit a different scaling with ρ (cf. Sec. 4.1).

We integrate the equations of motion with the time step $\Delta t = 91$ d, and the time span 4 Gyr. The output time step after computations of mean elements, proper elements, and final running-window filter is $\Delta t_{\rm out} = 10$ Myr.

2.5. Black-box method

We then proceed with a so-called 'black-box' method: (i) we choose 180 boxes with $\Delta a = 0.0243$ au, $\Delta e = 0.025$ in our case aligned with resonances[1]; (ii) count the numbers of observed asteroids located in these boxes; (iii) compute the observed differential SFD; (iv) the background differential SFD; (v) at every single output time step we compute the synthetic differential SFD (saving also lists of bodies in the respective bins); (vi) for every single size bin $(D, D + \mathrm{d}D)$ we draw a synthetic background population from a random uniform distribution (in $a_{\rm p}, e_{\rm p}, \sin I_{\rm p}$), because our volume is relatively small; if the background volume differs from our volume, we have to use a suitable factor f; (vii) we *rescale* the synthetic SFD to the observed one by randomly choosing $N_{\rm obs} - fN_{\rm bg}$ bodies from the lists above; (viii) we count the numbers of all synthetic asteroids located in the boxes; (ix) finally, we compute the metric

$$\chi^2 = \sum_{i=1}^{N_{\rm box}} \frac{(N_{{\rm syn}\,i} - N_{{\rm obs}\,i})^2}{\sigma^2_{{\rm syn}\,i} + \sigma^2_{{\rm obs}\,i}}\,, \qquad (1)$$

where the uncertainties are assumed Poisson-like, $\sigma = \sqrt{N}$. Using both $\sigma_{\rm obs}$ and $\sigma_{\rm syn}$ in the denominator prevents 'extreme' χ^2 contributions in boxes where $N_{\rm obs} \to 0$. We shall keep in mind thought the corresponding probability distribution of χ^2 may be somewhat skewed.

Unlike traditional simplified method fitting an envelope to (a, H) or $(a, 1/D)$, we obtain not only an upper limit for the age, but also a lower limit.

3. Results

Hereinafter, we discuss not only the best-fit model, but also several bad fits which are actually more important, because the 'badness-of-fit' assures a solid conclusion about Eos family.

[1] possibly also in $\sin I_{\rm p}$, or D

3.1. The nominal model

The nominal model is presented in Figure 6. We focus on the proper semimajor axis $a_{\rm p}$ vs proper eccentricity $e_{\rm p}$ distribution, having only one box in inclination $\sin I_{\rm p}$. The initial conditions (top left) are so different from the observations (bottom middle) it is almost hopeless to expect a good fit anytime in the future. However, at around $t = 1.3$ Gyr the situation suddenly changes (top middle); it is almost unbelievable that the synthetic family is so similar to the observations! The final state (top right) is again totally different. The χ^2 reaches values as low as $N_{\rm box}$, so we may consider the best fit to be indeed reasonable. The age interval is $t = (1.3 \pm 0.3)$ Gyr. Let us emphasize that the fit so good only because we carefully accounted for all three problems outlined in Section 2.

3.2. Bad fit 1: Ejection velocity tail

Because our sample is 3 times larger than the observed sample, we can easily resample our synthetic bodies without actually computing the N-body simulation anew, e.g. selecting only bodies with low ejection velocity $v_{\rm ej} < 200\,\mathrm{m\,s^{-1}}$. Initially, all bodies were located above the J7/3 resonance, and below the J11/5.

Using the same post-processing as above we arrived at Figure 7. It is clear that the 'best fit' is actually a poor fit compared to the nominal model. The notable differences are below the J7/3 resonance, and above the J11/5 where the numbers of bodies are never sufficient to match the observations (cf. Fig. 6, bottom middle).

It is worth to note there is small family just below the J7/3 resonance, namely (36256) 1999 XT_{17} (FIN 629). It seems aligned with the original velocity field of Eos family, it has the same $\sin I_{\rm p}$ as the family core, but slightly larger $e_{\rm p} \simeq 0.1$, because of the 'ellipse' in $(a_{\rm p}, e_{\rm p})$ visible in Fig. 6 (top left). We thus conclude, (36256) family is actually a *remnant* of the original velocity field.

If this is true, it may further contribute to the contamination of the 'pristine zone' between the J7/3 and J5/2 resonances, apart from low-probability crossings of the former resonance. This region was analysed by Tsirvoulis et al. (2017), where authors carefully subtracted the contribution of all families (including Eos), extracted the SFD of remaining background asteroids and computed the slope of the primordial (post-accretion) SFD.

3.3. Bad fit 2: Parent body inclination

If we look on contrary on the proper semimajor axis $a_{\rm p}$ vs proper inclination $\sin I_{\rm p}$ distribution (Figure 8) there is a problem with the nominal model. Inclinations are all the time too low (and the χ^2 too high compared to $N_{\rm box}$).

Nevertheless, it seems sufficient to adjust the inclination by approximately 0.005 rad to get a significantly better fit, χ^2 decreased from 238 down to 181. This seems still too high, but this approach is possibly too simplified, because we only shifted the output data. In reality, the resonances (in particular the z_1) do not shift at all, they are determined by the positions of giant planets, and we should perform the N-body integration anew to obtain a correct $(a_{\rm p}, \sin I_{\rm p})$ distribution.

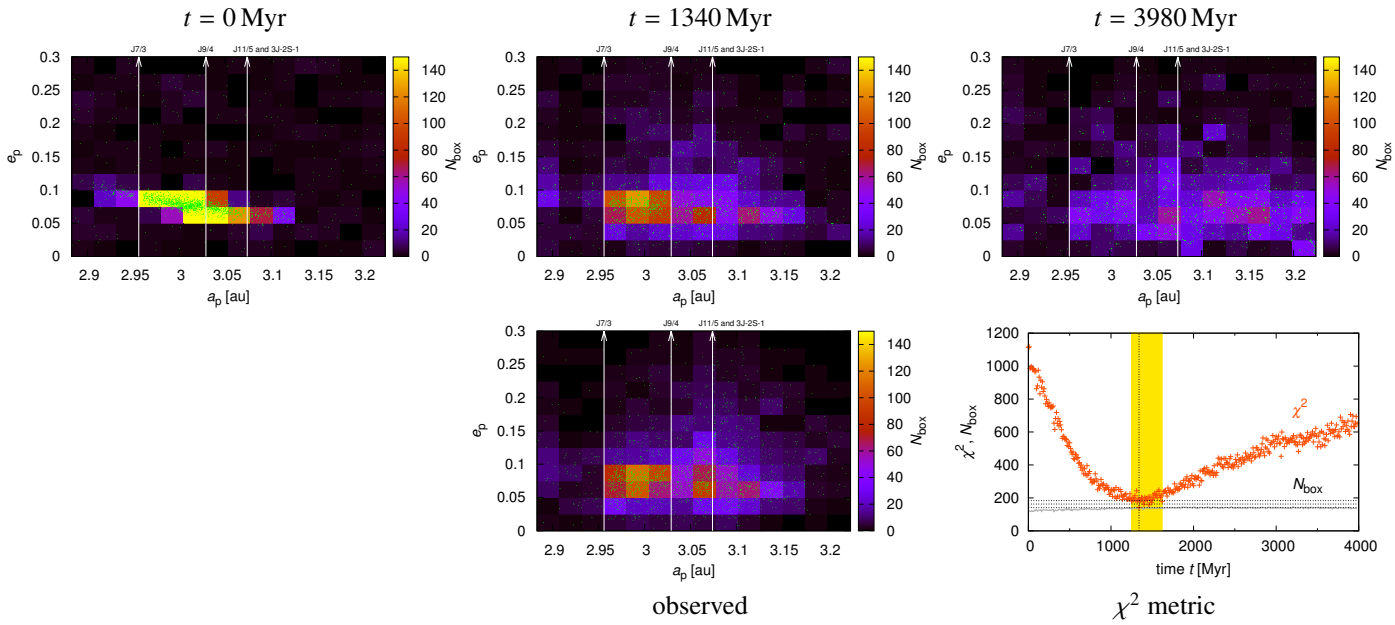

Figure 6: The proper semimajor axis a_p vs proper eccentricity e_p for the nominal simulation scaled to the observed SFD (as described in the main text) (top row). Bodies are plotted as green dots. Colours correspond to the number of bodies in 180 boxes, outlined by $\Delta a = 0.0234$ au, $\Delta e = 0.025$. The range of inclinations is always $\sin I_\mathrm{p} \in (0.06; 0.30)$. Positions of major mean-motion and 3-body resonances are also indicated (J7/3, J9/4, J11/5, and 3J – 2S – 1). The z_1 secular resonance goes approximately from the lower-left corner to the upper-right. There are the initial conditions (left column), the best-fit at $t = 1340$ Myr (middle), the end of simulation (right); as well as the observations (bottom middle), and the respective χ^2 metric compared to the actual number of boxes N_box (bottom right). The correspondence between the best-fit and the observations is surprisingly good, with $\chi^2 = 141$, $N_\mathrm{box} = 134$ (not all boxes are populated), and $\chi^2 \simeq N_\mathrm{box}$. The 1-$\sigma$, 2-$\sigma$ and 3-σ levels (dotted lines) and the inferred 3-σ uncertainty of the age (yellow strip) are indicated too.

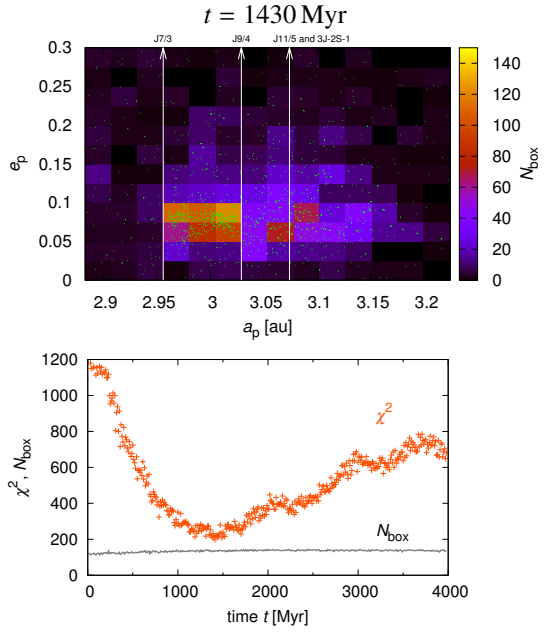

Figure 7: Bad fit 1: the proper semimajor axis a_p vs proper eccentricity e_p (top panel), and the temporal evolution of χ^2 (bottom panel) for a subset of bodies with the ejection velocities $v_\mathrm{ej} < 200\,\mathrm{m\,s^{-1}}$, i.e. without the tail of the distribution. Initially, all bodies were located above the J7/3 resonance. Observations are visible in Fig. 6 (bottom middle). The 'best-fit' at $t = 1430$ Myr, with $\chi^2 = 197$, $N_\mathrm{box} = 134$, is much worse than the nominal case. The number of bodies below the J7/3 resonance is too low. Consequently, the velocity tail is needed to get a better fit.

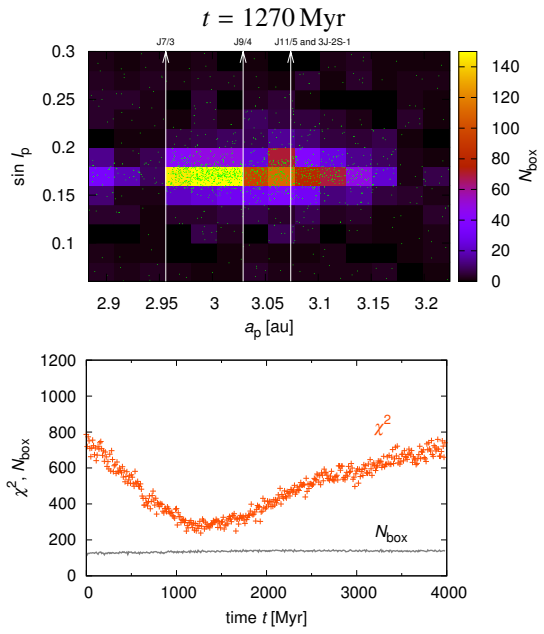

Figure 8: Bad fit 2: the proper semimajor axis a_p vs proper inclination $\sin I_\mathrm{p}$ for the synthetic population (top panel), and the temporal evolution of χ^2 (bottom panel). The boxes are consequently different, $\Delta a = 0.0243$ au, $\Delta \sin I = 0.02$, $e_\mathrm{p} \in (0.0; 0.3)$, so is the resulting 'best-fit' value $\chi^2 = 238$, $N_\mathrm{box} = 130$. The parent body would have to be shifted in inclination by approximately 0.005 rad to get a better fit.

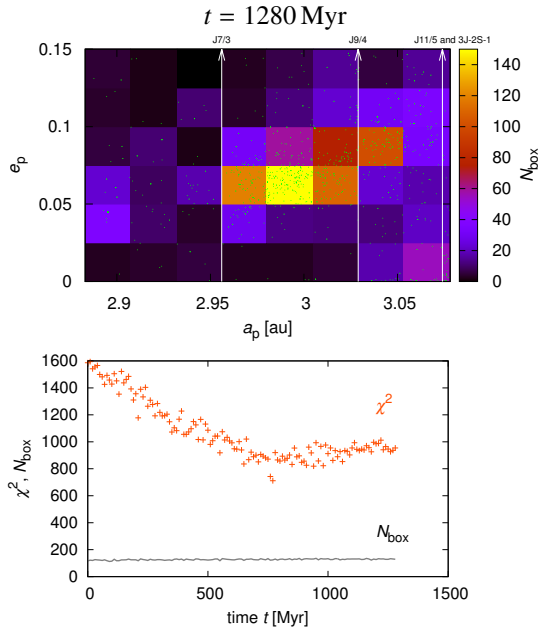

Figure 9: Bad fit 3: A detail of the proper semimajor axis a_p vs proper eccentricity e_p (top panel), and the temporal evolution of χ^2 (bottom panel) for the simulation with the true anomaly at the time of impact $f = 0°$, and the argument of perihelion $\omega = 30°$. The 'best-fit' $\chi^2 = 582$ is so high compared to $N_{box} = 67$ that the simulation was not computed up to 4000 Myr. The value has to be $f \gtrsim 120°$ to get a better fit.

3.4. Bad fit 3: True anomaly $f < 120°$

To demonstrate the sensitivity of our 'black-box' method with respect to the impact parameters, we present an alternative N-body simulation which started with the true anomaly $f = 0°$. The orientation of the ellipse is then the opposite and there is practically no chance for a good fit (see Figure 9).

All the time, there is a serious mismatch within the family core, it is impossible explain observed bodies in the box with $a_p \simeq 2.97$ au, and $e_p \simeq 0.08$. Generally, it is surprising that even 1.3 Gyr after the impact, there are clear traces of the original velocity field! As already reported in Brož and Morbidelli (2013), the 'true' true anomaly should be $f > 120°$.

4. Conclusions

Let us conclude, it is important to use a suitable selection of asteroids, match the size-frequency distributions, and account for the background population, when comparing N-body simulations with observations. To this point, we presented and tested a simple method how to fit a 3-dimensional distribution of proper elements.

For Eos family, it is possible to explain its shape in the $(a_p, e_p, \sin I_p)$ space and estimate the age at the same time, but this estimate still scales with the bulk density ρ, because most of the perturbations are non-gravitational (including all systematic drifts $\mathrm{d}a/\mathrm{d}t$, $\mathrm{d}e/\mathrm{d}t$, $\mathrm{d}I/\mathrm{d}t$).

While we believe our model include the key contributions, no dynamical model is complete. For example, we miss inner planets, gravitational perturbations by large asteroids, or short-term spin axis evolution due to gravitational (solar) torques. Initial condition might be also too simple. In particular, the velocity field might have been non-isotropic even though in catastrophic disruptions (like Eos) we rather expect a high degree of isotropy (Ševeček et al., 2017).

Generally, it is better to keep both as simple as possible to have the lowest possible number of free parameters. Let us at least compare our nominal best-fit model to another two distributions (size and spin) and the respective models (collisional and rotational).

4.1. Collisional evolution

In a Monte-Carlo collisional model, size-frequency distributions are evolved due to fragmentation and reaccumulation. We assume two populations, the main belt, and Eos family. Their physical parameters are summarized by the scaling law $Q^\star_D(r)$, for which we assume parameters of basalt at $5\,\mathrm{km\,s^{-1}}$ from Benz and Asphaug (1999). To compute the actual evolution, we use the Boulder code by Morbidelli et al. (2009). Parametric relations in the Boulder, which are needed to compute fragment distributions, are derived from SPH simulations of Durda et al. (2007).

We assume the initial SFD of the main belt relatively similar to the currently observed SFD, because we focus on the already stable solar system, with the fixed intrinsic impact probability $P_{imp} = 3.1 \times 10^{-18}\,\mathrm{km^{-2}\,yr^{-1}}$ and the mean velocity $v_{imp} = 5.28\,\mathrm{km\,s^{-1}}$. The initial SFD of Eos family has the same slope as the observed SFD in the range $D \in (15; 50)$ km, and it is prolonged down to $D_{min} = 0.005$ km. The dynamical decay time scale is taken from Bottke et al. (2005).

The resulting collisional evolution is shown in Figure 10. The observed knee at $D \simeq 15$ km is very important, because this usually arises from a collisional grinding. If we start with the constant slope from above, we can match the observed SFD at about 1300 Myr which is in accord with the dynamics.

It is worth to note the scaling with ρ is different from dynamics, which in principle allows to resolve the problem, however, the collisional model is sensitive to the initial conditions and using a slightly steeper SFD would result in longer age. In other words, everything is based on the simple assumption of the constant slope. It would be useful to base the initial conditions on a specific SPH model for Eos family, with the parent body size reaching up to 380 km (according to the simple scaling of Durda et al. 2007 results).

4.2. Spin distribution

At the same time, it is possible to fit the observed distribution of pole latitudes β, reported in Hanuš et al. (2018). If we use the same dynamical model, with the same post-processing, but focus on $(a_p, \sin\beta)$ boxes instead, we obtain the results summarized in Figure 11.

If we start from an isotropic distribution of spins, which means isotropic also in $\sin\beta$, after about 1.3 Gyr it is possible to fit both the asymmetry of the distribution with respect to $a_c = 3.014$ au, and the substantially lower number of bodies at mid-latitudes $|\sin\beta| < 0.5$. There are two systematics still

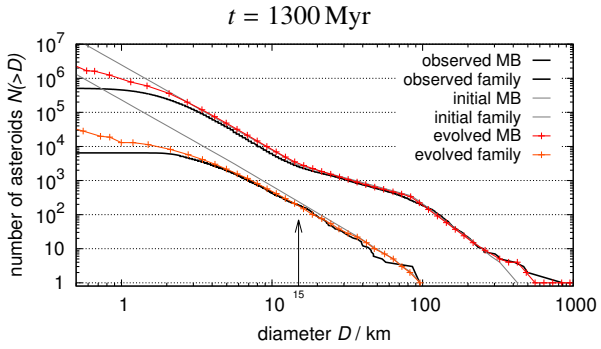

Figure 10: The cumulative size-frequency distributions computed by our Monte-Carlo collisional model of the two populations: main belt (red), Eos family (orange), together with the respective initial conditions (gray), and observations (black). At the time around $t = 1300$ Myr the correspondence is good, except the tail below $D \lesssim 2$ km, where an observational incompleteness makes the SFD's shallow. In particular, we successfully fit the knee of the family at $D \simeq 15$ km.

present in our analysis, as we account neither for the observational selection bias, nor for the bias of the inversion method.

Unfortunately, uncertainty is larger than in the previous case, because the number of observed bodies is limited, namely 46 within the family core. As a solution, we may use the distribution of $|\beta|$ of Cibulková et al. (2016) which is available for many more asteroids, but we would need to determine the PSF function for this (approximate) method, which smears the distribution substantially. The observed sample also contains a lot of bodies smaller than we had in the previous simulations, so we would have to compute everything again. This is postponed as a future work.

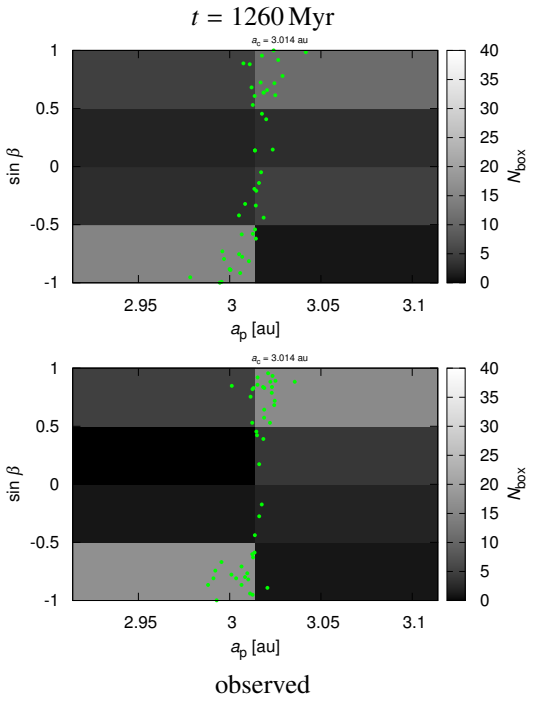

Figure 11: The proper semimajor axis a_p vs the sine of pole latitude $\sin\beta$ for the synthetic population (top panel), and the observed population of 46 bodies (bottom panel). The simulation started from initially isotropic distribution, i.e. isotropic in $\sin\beta$. The synthetic SFD was again rescaled to the observed one. We account neither for the observational selection bias, nor for the bias of the inversion method. Nevertheless, it is possible to fit both the asymmetry of the distribution with respect to $a_c = 3.014$ au, and the substantially lower number of bodies at mid-latitudes $|\sin\beta| < 0.5$.

Acknowledgements

The work of MB has been supported by the Grant Agency of the Czech Republic (grant no. P209-12-???). In this paper, we used observations made by BlueEye 600 robotic observatory, supported by the Technology Agency of the Czech Republic (grant no. TA03011171).

Benz, W., Asphaug, E., Nov. 1999. Catastrophic Disruptions Revisited. Icarus 142, 5–20.

Bottke, W. F., Durda, D. D., Nesvorný, D., Jedicke, R., Morbidelli, A., Vokrouhlický, D., Levison, H. F., Dec. 2005. Linking the collisional history of the main asteroid belt to its dynamical excitation and depletion. Icarus 179, 63–94.

Brož, M., Morbidelli, A., Apr. 2013. The Eos family halo. Icarus 223, 844–849.

Brož, M., Vokrouhlický, D., Morbidelli, A., Nesvorný, D., Bottke, W. F., Jul. 2011. Did the Hilda collisional family form during the late heavy bombardment? Mon. Not. R. Astron. Soc. 414, 2716–2727.

Cibulková, H., Ďurech, J., Vokrouhlický, D., Kaasalainen, M., Oszkiewicz, D. A., Nov. 2016. Distribution of spin-axes longitudes and shape elongations of main-belt asteroids. Astron. Astrophys. 596, A57.

Durda, D. D., Bottke, W. F., Nesvorný, D., Enke, B. L., Merline, W. J., Asphaug, E., Richardson, D. C., Feb. 2007. Size-frequency distributions of fragments from SPH/ N-body simulations of asteroid impacts: Comparison with observed asteroid families. Icarus 186, 498–516.

Farinella, P., Vokrouhlický, D., Hartmann, W. K., Apr. 1998. Meteorite Delivery via Yarkovsky Orbital Drift. Icarus 132, 378–387.

Hanuš, J., Delbo', M., Alí-Lagoa, V., Bolin, B., Jedicke, R., Ďurech, J., Cibulková, H., Pravec, P., Kušnirák, P., Behrend, R., Marchis, F., Antonini, P., Arnold, L., Audejean, M., Bachschmidt, M., Bernasconi, L., Brunetto, L.,

Casulli, S., Dymock, R., Esseiva, N., Esteban, M., Gerteis, O., de Groot, H., Gully, H., Hamanowa, H., Hamanowa, H., Krafft, P., Lehký, M., Manzini, F., Michelet, J., Morelle, E., Oey, J., Pilcher, F., Reignier, F., Roy, R., Salom, P. A., Warner, B. D., Jan. 2018. Spin states of asteroids in the Eos collisional family. Icarus 299, 84–96.

Hanuš, J., Ďurech, J., Brož, M., Warner, B. D., Pilcher, F., Stephens, R., Oey, J., Bernasconi, L., Casulli, S., Behrend, R., Polishook, D., Henych, T., Lehký, M., Yoshida, F., Ito, T., Jun. 2011. A study of asteroid pole-latitude distribution based on an extended set of shape models derived by the lightcurve inversion method. Astron. Astrophys. 530, A134.

Hirayama, K., Oct. 1918. Groups of asteroids probably of common origin. Astron. J. 31, 185–188.

Knežević, Z., Milani, A., Jun. 2003. Proper element catalogs and asteroid families. Astron. Astrophys. 403, 1165–1173.

Laskar, J., Robutel, P., Jul. 2001. High order symplectic integrators for perturbed Hamiltonian systems. Celestial Mechanics and Dynamical Astronomy 80, 39–62.

Levison, H. F., Duncan, M. J., Mar. 1994. The long-term dynamical behavior of short-period comets. Icarus 108, 18–36.

Masiero, J. R., Mainzer, A. K., Grav, T., Bauer, J. M., Cutri, R. M., Dailey, J., Eisenhardt, P. R. M., McMillan, R. S., Spahr, T. B., Skrutskie, M. F., Tholen, D., Walker, R. G., Wright, E. L., DeBaun, E., Elsbury, D., Gautier, IV, T., Gomillion, S., Wilkins, A., Nov. 2011. Main Belt Asteroids with WISE/NEOWISE. I. Preliminary Albedos and Diameters. Astrophys. J. 741, 68.

Morbidelli, A., Bottke, W. F., Nesvorný, D., Levison, H. F., Dec. 2009. Asteroids were born big. Icarus 204, 558–573.

Mothé-Diniz, T., Carvano, J. M., Bus, S. J., Duffard, R., Burbine, T. H., May 2008. Mineralogical analysis of the Eos family from near-infrared spectra. Icarus 195, 277–294.

Nesvorný, D., Brož, M., Carruba, V., 2015. Identification and Dynamical Properties of Asteroid Families. pp. 297–321.

Novaković, B., Tsirvoulis, G., Jul. 2014. Recent disruption of an asteroid from the Eos family. In: Muinonen, K., Penttilä, A., Granvik, M., Virkki, A., Fedorets, G., Wilkman, O., Kohout, T. (Eds.), Asteroids, Comets, Meteors 2014.

Parker, A., Ivezić, Ž., Jurić, M., Lupton, R., Sekora, M. D., Kowalski, A., Nov. 2008. The size distributions of asteroid families in the SDSS Moving Object Catalog 4. Icarus 198, 138–155.

Pravec, P., Harris, A. W., Nov. 2000. Fast and Slow Rotation of Asteroids. Icarus 148, 12–20.

Quinn, T. R., Tremaine, S., Duncan, M., Jun. 1991. A three million year integration of the earth's orbit. Astron. J. 101, 2287–2305.

Ševeček, P., Brož, M., Nesvorný, D., Enke, B., Durda, D., Walsh, K., Richardson, D. C., Nov. 2017. SPH/N-Body simulations of small (D = 10km) asteroidal breakups and improved parametric relations for Monte-Carlo collisional models. Icarus 296, 239–256.

Tsirvoulis, G., Morbidelli, A., Delbo, M., Tsiganis, K., Jun. 2017. Reconstructing the size distribution of the primordial Main Belt. ArXiv e-prints.

Čapek, D., Vokrouhlický, D., Dec. 2004. The YORP effect with finite thermal conductivity. Icarus 172, 526–536.

Šidlichovský, M., Nesvorný, D., Mar. 1996. Frequency modified Fourier transform and its applications to asteroids. Celestial Mechanics and Dynamical Astronomy 65, 137–148.

Vokrouhlický, D., Jul. 1998. Diurnal Yarkovsky effect as a source of mobility of meter-sized asteroidal fragments. I. Linear theory. Astron. Astrophys. 335, 1093–1100.

Vokrouhlický, D., Brož, M., Morbidelli, A., Bottke, W. F., Nesvorný, D., Lazzaro, D., Rivkin, A. S., May 2006. Yarkovsky footprints in the Eos family. Icarus 182, 92–117.

Vokrouhlický, D., Farinella, P., Dec. 1999. The Yarkovsky Seasonal Effect on Asteroidal Fragments: A Nonlinearized Theory for Spherical Bodies. Astron. J. 118, 3049–3060.

Zappalà, V., Bendjoya, P., Cellino, A., Farinella, P., Froeschlè, C., Aug. 1995. Asteroid families: Search of a 12,487-asteroid sample using two different clustering techniques. Icarus 116, 291–314.